



Experimental study of the grain-water mixture flow past a cylinder of different shapes

Sandro Longo^{a,*}, Alessandro Valiani^b, Luisfilippo Lanza^b, Dongfang Liang^c

^a Department of Civil Engineering, University of Parma, Parco Area delle Scienze, 181/A, 43124 Parma, Italy

^b Department of Civil Engineering, University of Ferrara, Via Saragat, 1, 44122 Ferrara, Italy

^c Cambridge University, Engineering Department, Trumpington Street, Cambridge CB2 1PZ, UK

ARTICLE INFO

Article history:

Received 8 May 2012

Received in revised form

27 August 2012

Accepted 1 November 2012

Available online 17 November 2012

Keywords:

Granular mixture

Sediment transport

Experiments

Resistance of bodies

ABSTRACT

This paper reports on the experiments of the flows of a mixture of grains and water around a circular or triangular cylinder, where the two-dimensional flow is driven by the internal cylinder of a Taylor–Couette cell. The working conditions during tests are such that instabilities do not appear. Velocity measurements of the mixture at the external surface are carried out using the PIV technique. The flow field is very different from that of a Newtonian fluid. However, the streamline patterns look similar, if the flow directions are ignored, as it happens for a dry granular stream. A limited recirculation zone behind the triangular cylinder is present, whose size is much less than that for a Newtonian fluid and is absent for dry granular stream. Upstream of the triangular cylinder, a zone of sediments almost at rest is present, with a semi-circular shape and an extension independent on the Reynolds number. It seems that the flow is controlled by factors downstream the location of interest. Vorticity scales with both the size of the obstacle and the free stream velocity, and is confined near the vertices at the base of the triangular cylinder. Compared to the vorticity field for the Newtonian fluid case, it spreads more upstream. The normalized energy of vortices has a probability distribution function with a peak and a steep reduction, but does not scale with the Reynolds number. The contribution of clockwise and counter-clockwise vortices is roughly balanced.

© 2012 Elsevier Masson SAS. All rights reserved.

1. Introduction

The granular flow around an obstacle is of interest in the study of the complex rheology of a fluid, as well as in practical applications. There are numerous industrial processes, where solid objects are present in the stream as heat exchanger or are used as weld lines in polymer processing applications. They are also relevant in food manufacturing, chemistry and pharmacy, and in measurements instrumentation, where the vortex shedding flow meter is based on the detection of shedding frequency of eddies generated by an obstacle inserted in the stream.

The literature includes several references on Newtonian fluid flows around a circular cylinder (see [1]), and the potential flow theory of infinitely long wings that uses conformal mapping of flow around a circular cylinder. [2] present a detailed analysis of the flow of water and polymer additive around a circular cylinder, while [3] analyze the gravity-driven flow of mustard seeds around a cylinder, adopting a kinematic description based on a stochastic

model. Other more detailed analyses refer to the kinematics of complex fluids flows around bodies [4].

Despite the widespread use of cylindrical and non-circular obstacles in many applications, the studies on this geometry effect are scant, especially for triangular cylinder with a vertex facing downstream.

There are limited experimental and theoretical analyses for Newtonian fluids with the numerous possible conditions (orientation respect to the incoming flow, characteristics of the incoming flow, aspect ratio of the obstacles, etc.), let alone non-Newtonian fluids. [5] numerically analyzed the flow of incompressible Newtonian fluids around a triangular cylinder with the apex facing upstream, while [6] made an extensive numerical simulation for the 2-D laminar flow of power-law fluids over an equilateral triangular cylinder in both configurations, i.e. with apex facing upstream and downstream. A few experimental investigations about the shedding vortices from the triangular cylinders or prisms in cross flow have been reported in high Reynolds-number turbulent flows, e.g. [7–10].

The present experiments deal with a mixture of grains and water – a fluid with a complex rheological behavior. A crude analogy can be made between this flow with the dry granular flow, with air as inter particles fluid. Usually, numerical simulation is

* Correspondence to: Cambridge University, Engineering Department, Cambridge, UK. Tel.: +39 0521 905157; fax: +39 0521905924.

E-mail address: sandro.longo@unipr.it (S. Longo).

Nomenclature

\dots^*	Non dimensional operator
δ	Thickness of the gap
Γ	Shear rate, circulation
λ	Linear concentration of the solid phase, eigenvalue
μ	Dynamic interparticle fluid viscosity
ν	Kinematic viscosity of the interparticle fluid
$\nu_{mixture}$	Apparent kinematic viscosity of the mixture
ρ_s	Mass density of the solid phase
σ	Standard deviation
ω, ω_z	Rotation rate, vorticity component along z
Ω	Tensor, antisymmetric part of the velocity gradient tensor
$a_1, b_1, c_1, d_1, e_1, a_2, b_2, c_2, d_2, e_2, c$	Coefficients
b	Length of the edge of the base of the triangular cylinder
Ba	Bagnold number
C, C_0	Void concentration of the grains (ratio between the volume of sediments and the bulk volume), maximum void concentration of the grains
CCW	Counterclockwise
CW	Clockwise
d	Grain diameter
D	Diameter of the circular cylinder, of the cylinder of the cell (internal or external)
E	Energy
FOV	Field of view
l_k	Length of the kernel
L	Length of the recirculating zone
$L_{x,y}(\dots)$	Polynomials for spatial correction along x, y
LDA	Laser Doppler Anemometry
NDH	Nedderman R.M., Davies S.T., Horton D.J. (1980), Powder Technology 25 215–223
pdf	Probability density function
PIV	Particle Image Velocimetry
PMMA	Polymethyl methacrilate
POD	Proper Orthogonal Decomposition
R, r	Radius of the cylinder (internal, external) radius of the eddies
rpm	Revolutions per minute
Re, Re_c	Reynolds number, critical Reynolds number
\mathbf{S}	Tensor, symmetric part of the velocity gradient tensor
s	Wall thickness
t, dt	Time, time increment
Ta, Ta_c	Taylor's number, critical Taylor's number
U_0	Reference asymptotic velocity
U_x, U_y	Horizontal, vertical instantaneous velocity
U, V	Horizontal, vertical instantaneous velocity
U'_x, U'_y	Horizontal, vertical fluctuating velocity
U', V'	Horizontal, vertical fluctuating velocity
x, y	Spatial co-ordinates
\mathbf{x}, \mathbf{x}'	Position vector, dummy position vector
x_c, x_m, y_c, y_m	Spatial co-ordinates measured, corrected

free path of particles and the diameter of the cylinder. They also depicted some properties of the granular flow, including velocity, temperature (a measure of the velocity fluctuations) and the solid fraction field. [12] experimentally studied the flow around a fixed cylinder immersed in a uniform dry and dense granular flow, including the vorticity and the granular temperature fields. They found that the drag force is independent of the mean flow velocity and scales with the asymptotic stress.

The drag behaves differently between the obstacles moving in the granular medium at rest and the obstacles at rest placed in a granular stream. In both cases, the presence of grains at high concentrations near the obstacles induces stress transmission through contact forces and leads to a jammed state. This jammed state is a character of granular flows, different from classical Newtonian fluid flows. Jamming can be caused by the gravity force and compressive stress. The main kinematic effect of jamming is the need for a proper re-organization of the flow pattern around obstacles inside a granular medium. The length scale of the re-organization pattern is different in the two extreme situations and generally enhances the disturbances by the obstacles, which subject strong fluctuations of the drag force. If the granular medium is at rest (on average), the drag usually depends little on the speed or on the form of its cross-section [13], except at low velocities. If the obstacle is at rest, a much stronger dependence on granular velocity is expected, with a low resistance similar to that for a usual fluid (a quadratic law at high velocities). These results can be drastically different if a lubricant interstitial fluid is present. Some numerical experiments on the interaction of a stream of granular particles with a resting obstacle in two dimensions [14] show that, at low velocities, the drag is proportional to the $3/2$ power of the velocity, whereas at high velocities, the drag recovers its usual quadratic dependence on velocity.

Compared to other flows, granular flows are often characterized by significant variations in bulk density. Experiments by [15] show that a granular stream impacting an obstacle or being regulated by a wall has different zones of compression and expansion with shocks and discontinuities. In these experiments, it is very difficult to measure fluid velocity. It is possible to use Laser Doppler Anemometry (LDA) [16] and Particle Image Velocimetry (PIV) [17] through a transparent wall. While PIV exactly displays the particle motion, results usually underestimate the real velocity due to the wall boundary layer (unless it is used for measuring a free granular surface), but fortunately, this error is limited due to slip of granular flows at the boundary.

The flow of a fluid–granular mixture is characterized by three main regimes: (i) a macroviscous regime with essentially Newtonian behavior, (ii) a dilatant regime with interparticle collisions dominant, and (iii) a quasi-static regime, with stresses transferred mainly as frictional stresses. Several models have been developed and tested for dry grain rapid granular flows, mainly based on the assumption of an isotropic granular temperature, small dissipation and low to mid grain void ratio. Significant progress has also been made regarding the granular temperature anisotropy. However, little has been done to include the effects of interstitial fluid since Bagnold's pioneering work [18]. Bagnold was interested in the rheology of the mixture, and developed a model widely used for its simplicity that makes it an excellent tool for practical computations or simplified approaches. Despite several critics [19] and the limitations of the model (e.g., the evidence that it does not develop a constitutive equation, lacking a tensorial formulation), Bagnold's model is still adopted at least for concentrated suspensions of grains in water at low shear rates (Bagnold's macroviscous regime). However, Bagnold's model does not consider the interaction between the mixture and solid boundaries.

The aim of the present experiments is to provide information on the kinematics of the flow fields past a circular cylinder and a

used for studying granular flows, and in most analysis the drag of obstacles in the granular stream is of major interest. [11] used discrete element simulations to investigate a two-dimensional dilute dry granular flow around an immersed cylinder (no interparticle fluid) in order to evaluate the drag coefficient. They found that the drag coefficient depends on the Mach number, expressed as the ratio of the asymptotic velocity and the celerity of sound, and on the Knudsen number, expressed as the ratio between the mean

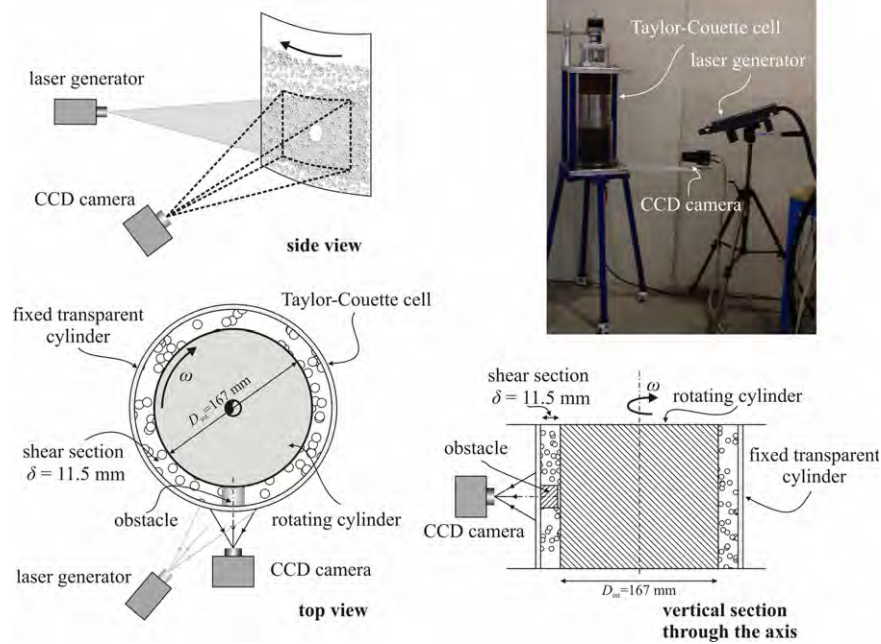


Fig. 1. Experimental set up.

triangular cylinder immersed in a fluid–granular mixture stream with grains at high void concentrations, including the analysis of isolated vortices. The tests with the circular cylinder have been partially analyzed in [20]. Compared to most experiments in the literature, the presence of the water as the inter-particle fluid represents a significant variation, since only physical [3,12] and numerical experiments (e.g. [21]) with either dry grains or homogeneous non Newtonian fluids have been documented [4]. Such mixtures are common in environmental flows (but at higher Reynolds number), like debris flows, and in the industry, like fluidized beds for chemical reactions. The device used to generate the stream is a Taylor–Couette cell, which, in the working conditions during the tests, is far from the instability development level. Momentum is transferred from the internal rotating cylinder through collisions with the grains of the mixture and through a (limited) wall stress acting on the fluid phase. The device is easy to control and does not suffer from the limitations typical of channels with recirculating mixture, like varying void concentration of the grains and free surface instabilities. The use of almost neutrally buoyant grains limits gravity effects that would induce a normal stress increase with depth. Note that gravity, which acts as a source of momentum in a gravity channel, is a disturbing effect in this device because it favors particle segregation and grain void variation.

In Section 2, we describe the experimental set-up and the measurement techniques. In Section 3 we describe the techniques for data analyses. In Section 4 there is the presentation and discussion of the experimental results, with the description of the flow field, including the vorticity, with the details on the vortices statistics. Conclusions are reported in the last section.

2. Methodology

2.1. Experimental setup

Experiments were performed in a concentric-cylinder Taylor–Couette shear cell (Fig. 1), with an internal rotating vertical cylinder made of stainless steel with a diameter $D_{\text{int}} = 167$ mm and an external fixed cylinder made of Polymethyl methacrylate (PMMA) with a diameter $D_{\text{ext}} = 190$ mm. The radius ratio is equal

to $D_{\text{ext}}/D_{\text{int}} = 1.137$. The height of the cell is 340 mm, the wall thickness of the external fixed cylinder is $s = 5$ mm and the annular gap between cylinders, representing the shear section, is $\delta = 11.5$ mm. The internal cylinder is in motion, in order to transfer momentum to the granular mixture. Its wall is roughed by gluing sandpaper to it. The sandpaper has a roughness comparable with the size of the grains; its overall thickness is less than 1 mm.

The internal surface of the PMMA cylinder is smooth and allows almost free slip of the grains. The driving mechanism for the stainless-steel internal cylinder is a stepper with a resolution of 0.36 degrees per step, controlled by a computer and connected to a coaxial mechanical gear 1:6 in order to increase the torque. The gear reduction also increases the resolution of the driving mechanism to 0.06 degrees per step of the internal cylinder.

Tests were carried out with a mixture of water and artificial clay grains used for thermal insulation purposes, whose commercial name is Leca. The grains were sorted to have a diameter of $d = 0.25$ – 0.50 mm. They are almost spherical and have a specific weight nearly equal to 1.0. This low value is due to the presence of air trapped in the particles during the production process. Sorting for the specific weight was necessary to eliminate floating particles. The choice of almost neutrally buoyant particles is necessary to reduce to a minimum the normal effective stress increment due to gravity, which would reduce grain mobility, especially in the deeper layers.

The maximum solid fraction, defined as the ratio between the volume of sediments and the bulk volume, for random packing was determined by measuring the bulk volume of the grains at rest, the weight of the sample and the specific weight, obtaining a value of $C_0 = 0.643$. During motion, the solid fraction is reduced due to particle dilatancy and resuspension, achieving a computed mean value of granular void concentration of $C \approx 0.56$.

2.2. Measurements

Measurements were carried out in the Laboratory of Civil Engineering “Paolo Lamberti” of the University of Ferrara, using a commercial TSI PIV with a 2048×2048 pixel² Video camera TSI Power View Model 630149, fitted with a NIKOR AF D 50 mm/f lens with an adaptor ring Nikon PK-12, which increases the focal

by 14 mm. The light source was a Solo Nd:YAG III dual laser head with maximum repetition rate of 15 Hz and output energy of 50 mJ. It was water-cooled and mounted on the same side of the video camera. The layout is shown in Fig. 1.

Usually, the laser passes a cylindrical lens to generate a light sheet. For the present purposes, the lens was removed and substituted with two cylindrical lenses in series and with mutually orthogonal axis in order to enlarge the beam, transforming the laser beam in a light spot able to illuminate the area detected in the frames of the videocamera. Polarized lenses were added to the video camera in order to eliminate reflections.

The laser light illuminates frontally the particles moving near the transparent wall of the cell and only occasionally can reach the second layer of particles, with a probability to go further in depth reduced at high grain concentration. Hence most of the signal is scattered by the particles near the wall. The position of the camera and the lens focus were chosen in order to have a depth of field of 20 mm that ensures an acceptable sharpness of the image in all frames. We checked the overall performances of the measurement system by gluing a sheet of paper with random dots to a rotating circular plate moved by the stepper motor, exactly in the same configuration of the tests. The measured velocity was within 1% of the expected values.

The acquisition frequency of a couple of images was 3.75 Hz, with a time interval between the two images ranging from 600 to 1000 μ s depending on the maximum particle velocity and gradient of velocity. In the tested condition, PIV measures the velocity of the grain particles, which appear much brighter than the small particles present in the interstitial fluid.

The curvature of the PMMA cylinder and the refraction generate image distortion. An additional distortion is due to the lenses of the video camera. We performed a numerical correction to the acquired data. The algorithm is about the transformation of the pixel position on the CCD of the camera onto metric position in the plane space equivalent to the rolled cylinder surface.

The transformation is in terms of quadratic polynomials:

$$\begin{cases} x_c/x_m = L_x(x_m, y_m) \equiv a_1x_m^2 + b_1y_m^2 + c_1x_m + d_1y_m + e_1 \\ y_c/y_m = L_y(x_m, y_m) \equiv a_2x_m^2 + b_2y_m^2 + c_2x_m + d_2y_m + e_2 \end{cases} \quad (1)$$

used to correct both coordinates. The subscript c and m indicate 'corrected' and 'measured' respectively, L_x and L_y are the polynomial operators symbols adopted for correcting the two coordinates, and the dimensional coefficients of the polynomials are estimated using the best-fit criterion.

Calibration of the geometry of the field of view (FOV) follows these steps: (1) acquisition with the video camera of a regular grid stuck on the external surface of the PMMA cylinder. (2) Estimation of the coordinates (in pixels) of the grid nodes, using the acquired image. (3) Minimization of the residuals. The estimated coefficients have an uncertainty of $\approx 2\%$ at the 95% confidence level and little correction is needed in the central part of the FOV.

Velocity computation was carried out by adopting the TSI software based on correlation analysis of two different frames, by using an interrogation window of 32×32 pixel² ($\approx 8 \times 8d^2$) with 50% overlap. The result is a matrix of vectors at the grid nodes, 16 pixels apart, corresponding to 1.25 mm ($\approx 4d$).

The output files contain the coordinates (in pixels) of the interrogation window and the two components of the space vector at time t (first frame) and $t + dt$ (subsequent frame). For easy use and subsequent elaboration, the matrix is interpolated by a regular grid with square side length equal to 1.25 mm. For each test, 100 couples of frames were acquired, corresponding to about 27 s long. After the correlation analysis was complete, outliers were rejected using the cellular neural network method [22]. The percentage of vectors rejected varied from 6% to 16%.

3. Data analyses and experimental cases

In the following, a brief explanation of the Proper Orthogonal Decomposition (POD) and of the technique for vortex detection is given.

3.1. The proper orthogonal decomposition (POD)

The POD analysis was first suggested in fluid mechanics by [23], but also has separate applications and development in numerous other fields. The snapshot method [24] is used.

Given a series of N snapshots, the fluctuating part of the i th snapshot is computed by subtracting the ensemble average:

$$\mathbf{U}'^{(i)}(\mathbf{x}) = \mathbf{U}^{(i)}(\mathbf{x}) - \frac{1}{N} \sum_{j=1}^N \mathbf{U}^{(j)}(\mathbf{x}). \quad (2)$$

The fluctuating parts of velocity components for the N snapshots are rearranged as:

$$\mathbf{W}(\mathbf{x}, t) = [\mathbf{U}'^{(1)} \mathbf{U}'^{(2)} \dots \mathbf{U}'^{(N)}] = \begin{bmatrix} U_1'^{(1)} & U_1'^{(2)} & \dots & U_1'^{(N)} \\ \vdots & \vdots & \vdots & \vdots \\ U_{lm}'^{(1)} & U_{lm}'^{(2)} & \dots & U_{lm}'^{(N)} \\ V_1'^{(1)} & V_1'^{(2)} & \dots & V_1'^{(N)} \\ \vdots & \vdots & \vdots & \vdots \\ V_{lm}'^{(1)} & V_{lm}'^{(2)} & \dots & V_{lm}'^{(N)} \end{bmatrix} \quad (3)$$

where for simplicity the dependence on \mathbf{x} of the fluctuating velocities $\mathbf{U}'^{(1)}, \mathbf{U}'^{(2)}, \dots, \mathbf{U}'^{(N)}$ has been omitted. The time dependence of $\mathbf{W}(\mathbf{x}, t)$ is transformed into dependence on the N snapshots taken at different times. If the velocity components are stored in a $l \times m$ matrix like in a PIV frame, the matrix is reshaped into a column vector of length $l \times m$ and the dependence on \mathbf{x} is expressed by the subscript. After calculating the $N \times N$ autocovariance matrix $\mathbf{C} = \mathbf{W}^T \mathbf{W}$ we solve the eigenvalue problem

$$\mathbf{C} \mathbf{A}^i = \lambda^i \mathbf{A}^i. \quad (4)$$

After sorting the N eigenvalues in descent order, with $\lambda^1 > \lambda^2 \dots > \lambda^N$, the normalized modes of the decomposition are:

$$\varphi^i(\mathbf{x}) = \frac{\sum_{n=1}^N A^{i(n)} \mathbf{U}^{(n)}}{\left\| \sum_{n=1}^N A^{i(n)} \mathbf{U}^{(n)} \right\|} \quad i = 1, 2, \dots, N, \quad (5)$$

where $A^{i(n)}$ is the n th component of the normalized eigenvector corresponding to the i th eigenvalue λ^i . The modes are function of the space \mathbf{x} . These are an optimal base of the functional space that includes the N snapshots, in the sense that any reconstruction using another basis with the same number of modes contains less energy. It is also the most efficient way of extracting the most-energetic components of an infinite-dimensional process with only a few modes [25]. The modes are independent (orthogonal), complete (describe the entire functional space) and are normalized. The i th component of the generic n th snapshot is computed by projection of the raw velocity fields on the POD basis:

$$a^{i(n)} = \varphi^i \mathbf{U}'^{(n)} \quad (6)$$

and

$$\mathbf{a}^{(n)} = \boldsymbol{\Psi}^T \mathbf{U}^{(n)}, \quad (7)$$

where $\boldsymbol{\Psi} = [\varphi^1 \varphi^2 \dots \varphi^N]$. For each snapshot the number of components is equal to the number of modes. Different snapshots have different components on a given mode, so the component varies in

time. The n th snapshot is obtained by summing the reconstructed fluctuating part to the ensemble average:

$$\begin{aligned} \mathbf{U}^{(n)}(\mathbf{x}) &= \sum_{i=1}^N a^{i(n)} \varphi^i + \frac{1}{N} \sum_{j=1}^N \mathbf{U}^{(j)}(\mathbf{x}) \\ &\equiv \boldsymbol{\Psi} \mathbf{a}^{(n)} + \frac{1}{N} \sum_{j=1}^N \mathbf{U}^{(j)}(\mathbf{x}). \end{aligned} \quad (8)$$

If only the first m eigenmodes are included, the n th snapshot has the approximate expression:

$$\mathbf{U}^{(n)}(\mathbf{x}) \approx \sum_{i=1}^m a^{i(n)} \varphi^i + \frac{1}{N} \sum_{j=1}^N \mathbf{U}^{(j)}(\mathbf{x}). \quad (9)$$

An eigenvalue represents the energy associated to its corresponding mode, hence the first modes, after sorting, are the most energetic. The number of modes to include in the approximate reconstruction is not only related to the content of energy to save in the snapshot but also depends on the complexity of the flow. [26] suggests that at least 90% of the energy should be included, with any residual mode carrying less than 1%. Amongst some important properties of the POD is that both original velocity fields and empirical eigenmodes respect the same boundary conditions. Hence, it is not necessary to constraint the empirical eigenmodes in order to satisfy the boundary conditions.

In many cases, the POD applied to vorticity or to enstrophy is more efficient, first because the number of elements is halved respect to the two-components velocity (in 3-D analysis there is no advantage), second because in some flows a smaller number of modes is requested for reconstruction. A discussion on the appropriate variable to be used in POD analyses is given in [27].

3.2. The detection of vortices

The definition of a vortex is itself variegated and its detection is based on different approaches. The simplest definition of a vortex is probably given by [28] and has also been practically adopted by [29] and others. The streamlines of a vortex look roughly circular or spiral in a reference moving with the core, hence it is necessary to look for these patterns in the instantaneous flow. For this aim, it is first necessary to remove the low frequency components, including the mean motion, which can be orders of magnitudes stronger than the vortices.

Among the approaches, which give the criteria to identify a vortex, we list the following, which are not exhaustive: (1) using the eigenvectors' characteristics in a phase-plane analysis [30]; (2) verifying the spatial correlation of the vorticity [31]; (3) λ_2 -criterion [32]; (4) computing two ad hoc functions based on the proper orthogonal decomposition [33].

The present approach adopts the λ_2 -criterion given by [32] with a revised identification methodology, partially based on [29] approach.

The first step is removing the mean motion, so a low pass Gaussian filter is applied to the flow field:

$$\mathbf{U}_{lp}(\mathbf{x}, t) = \int_D g(\mathbf{x} - \mathbf{x}') \mathbf{U}(\mathbf{x}', t) d\mathbf{x}' \quad (10)$$

where

$$g(\mathbf{x} - \mathbf{x}') = \exp\left(-\frac{|\mathbf{x} - \mathbf{x}'|^2}{2\sigma^2}\right), \quad (11)$$

where \mathbf{x}' is the dummy position vector and σ is the standard deviation of the filter, which is a measure of its size. Then the high-pass velocity component is equal to

$$\mathbf{U}_{hp}(\mathbf{x}, t) = \mathbf{U}(\mathbf{x}, t) - \mathbf{U}_{lp}(\mathbf{x}, t) \quad (12)$$

and exposes possible vortices. The choice of the standard deviation of the filter also decides the minimum number of points around to be included in filtering, since the kernel of the filter has length equal to $l_k = 6\sigma - 1$. If $\sigma = 2$ grid units, then $l_k = 11$ grid units and it is necessary to include at least 6 points around the local origin. The cut off length of the Gaussian filter is not defined, since its length response in Fourier space is still a Gaussian function continuously decaying. But clearly, it is a fraction of the length of the kernel and, in this application, it limits the maximum radius of the vortices that can be identified.

The application of vortex detection on a structured grid data requires the selection of the possible center of a vortex coincident with a grid point of measurements; then the radius of first attempt can be equal to 1 grid step and the second radius can be $\sqrt{2}$ grid steps, the third can be 2 grid steps, etc., using only surrounding points of the possible center. Instead of being tied to the grid nodes, it is more efficient and also applicable to non structured grid data, to implement the interpolation of the velocity field onto points on a circle of arbitrary radius, by using an interpolation method. After careful checking of the performances of the algorithm, comparing the response with a set of synthetic PIV data including known Rankine vortices, we chose $\sigma = 2\sqrt{\Delta x \cdot \Delta y}$ and limited the surrounding points for interpolating the velocity to ± 6 grid points in both directions.

For a given radius, the detection algorithm evaluates the angle between the velocity in several nearby points equally spaced and the local tangent. If at least 6 of the 8 angles are within the range $\pm 30^\circ$ or 150° – 210° , a second check is done with respect to the variability of the velocity, which must be within a standard deviation. If at least 6 out of 8 vectors satisfy the criteria, a positive case is detected and stored.

The analysis is repeated for each frame and for increasing radius, and a mask is used to prevent the inclusion in the analysis of points inside the solid body. It frequently happens that in the same frame and in the same location two or more vortices with increasing radius are identified. Assuming that they are the same vortex scanned at different distances from its center, a post processing retains only the vortex with the largest radius. For all the detected vortices, the circulation is computed as:

$$\Gamma = \oint \mathbf{U}_{hp} \cdot d\mathbf{s}, \quad (13)$$

where $d\mathbf{s}$ is the infinitesimal vector tangent to the circle. All the detected vortices are stored with the coordinates of their center, with the value of their energy proportional to the squared circulation

$$E = c\Gamma^2, \quad (14)$$

where c is a coefficient, and with their orientation, i.e. clockwise (CW) and counter-clockwise (CCW) vortices.

The next step is to check if these vortices satisfy [32] condition, also known as λ_2 -criterion. λ_2 is the second largest eigenvalue of the tensor $\mathbf{S}^2 + \boldsymbol{\Omega}^2$, where \mathbf{S} and $\boldsymbol{\Omega}$ are the symmetric and antisymmetric parts of the velocity gradient tensor, respectively. This value has negative value where a minimum of pressure is reached, usually in the core of a vortices. The criterion can be applied to 3-D flows, but has a 2-D flows expression. The value of λ_2 in a 2-D flow field is:

$$\lambda_2 = \left(\frac{\partial U}{\partial x}\right)^2 + \left(\frac{\partial V}{\partial x}\right) \left(\frac{\partial U}{\partial y}\right). \quad (15)$$

The limitations of this criterion arise from the possible three dimensionality of the flow field and the apparent compressibility of the present fluid. In fact, the density of the grains is not rigorously uniform, but has largest value where grains are almost at rest and a minimum value where strong shearing is present.

Table 1
Set of experiments with a circular cylinder (see [20]).

Imposed rotation rate (rpm)	Computed lateral velocity of the driving wall (mm/s)	Measured asymptotic velocity of flow U_0 (at the transparent wall) (mm/s)	Mean radial shear rate (s^{-1})	Bagnold number (.)	Reynolds number (.)
50	440	305	11.7	7.5	36
100	880	615	23.0	15	72
150	1320	920	34.8	22	108
200	1760	760	87.0	56	89

Table 2
Set of experiments with a triangular cylinder.

Imposed rotation rate (rpm)	Computed lateral velocity of the driving wall (mm/s)	Measured asymptotic velocity of flow U_0 (at the transparent wall) (mm/s)	Mean radial shear rate (s^{-1})	Bagnold number (.)	Reynolds number (.)
25	220	194	2.3	1.5	20
50	440	356	7.3	4.6	36
100	880	554	28.3	18	56
150	1320	752	49.4	31	77
200	1760	912	72.9	46	94

3.3. The experiments

In this series of tests, two different obstacles are considered: the first one is a circular cylinder with a diameter equal to 15 mm and a height of 9 mm. The second one is an equilateral triangular cylinder with an edge length of the base equal to 13 mm and the same height of the circular cylinder. The triangle could be circumscribed in the circle. The bases of the obstacles are glued to the internal surface of the PMMA cylinder and are located 50 mm above the bottom of the Taylor–Couette cell. The free surface of water at rest is at 150 mm above the bottom, while the grain bottom is 20 mm below the free surface. A gap of a few millimetres is present between the obstacle and the internal rotating cylinder in order to avoid particle locking. At the maximum rotation rate of the internal cylinder, the mixture is almost homogeneous, with the mean void concentration of the mixture equal to $C = 0.557$, i.e. reduced to 87% of the value at rest.

Measurements were carried out with a rotation rate from 50 to 200 rpm (a single set at 25 rpm is also available only for the triangular cylinder experiments), corresponding to a lateral velocity of the internal cylinder from 440 to 1760 mm/s. Some initial tests without any obstacle show a quite regular flow field, with limited shearing in the radial direction and in the horizontal plane. By moving the internal cylinder, the measured sediment velocity at the external wall (asymptotic value), a theoretical mean value of the shearing rate in the radial direction is computed. The data are shown in Tables 1 and 2 for the circular and the triangular cylinder, respectively.

The actual mean value of the shearing rate in the radial direction is less than the theoretical, due to the existence of a boundary layer near the driving wall where the pseudotemperature level is high, with a consequent reduction of grain concentration. The bouncing of the sediments facilitates slip. Hence an almost uniform flow is obtained in radial direction, with minimal effects of curvature of the trajectories due to the annular gap. At 200 rpm, with a circular cylinder in place, the measured velocity of the grains near the external cylinder is surprisingly smaller than that measured at 150 rpm (see Table 2), presumably due to emerging instabilities in the flow field even though the Taylor number is below the critical value.

In order to qualify the flow regime, we introduce the Bagnold number, defined as

$$Ba = \frac{\rho_s d^2 \lambda^{1/2} \Gamma}{\mu}, \quad (16)$$

where ρ_s is the density of the solid phase, d is the particle diameter, λ the linear concentration of the solid phase, Γ the shear rate and μ

the inter particle fluid viscosity. The linear concentration is related to the solid void concentration by

$$\lambda = 1 / [(C_0/C)^{1/3} - 1]. \quad (17)$$

In Bagnold's model, the limit for quadratic variation of the stress is $Ba > 450$. Computing the Bagnold number by using the radial shear rate results in values in the macroviscous regime or at most in transitional regime.

To compute the Reynolds number, defined as

$$Re = \frac{U_0 D}{\nu_{mixture}} \quad \text{or} \quad Re = \frac{U_0 b}{\nu_{mixture}} \quad (18)$$

for the circular cylinder and for the triangular cylinder, where b is the edge length of the base, we assume a kinematic viscosity of the mixture equal to

$$\nu_{mixture} = 2.2 \lambda^{3/2} \nu. \quad (19)$$

A Taylor–Couette flow can be unstable. The Taylor number, defined as:

$$Ta = \frac{\omega^2 R_{int} (R_{ext} - R_{int})^3}{\nu^2} \quad (20)$$

is the ratio between centrifugal forces and viscous forces and is used to quantify the limit of stability. The critical Taylor number for the appearance of the first unstable modes is equal to $Ta_c \approx 1700$ [34]. By assuming a pure Newtonian fluid viscosity it results that the first instabilities arise at a rotation rate equal to $\omega_c = 0.1157 \text{ rad/s} \approx 1.1 \text{ rpm}$. By assuming the equivalent viscosity of the mixture it results $\omega_c = 23.37 \text{ rad/s} \approx 223 \text{ rpm}$, slightly larger than the maximum rotation rate of the experiments. Hence in the conditions of the present experiments the flow is always stable. These results should be considered with care, since it is not demonstrated that the Taylor–Couette instability for a granular mixture has the same critical number of the correspondent instability for a Newtonian fluid. A further uncertainty arises in the value of the equivalent viscosity of the mixture.

A complete analysis would require the modification of the significant non dimensional parameters by also modifying the inter-particle fluid viscosity, the relative size of the grains and of the obstacle, the roughness of the lateral walls of the obstacles, eventually the elasticity of the grains and the static angle of repose. Considering the limitations of the experimental apparatus, most of these variables cannot be easily modified and only the variation of the inter-particle fluid viscosity is planned for further tests. Referring to the relative size of the grain particles respect to the size of the obstacle, it is expected that it becomes important if

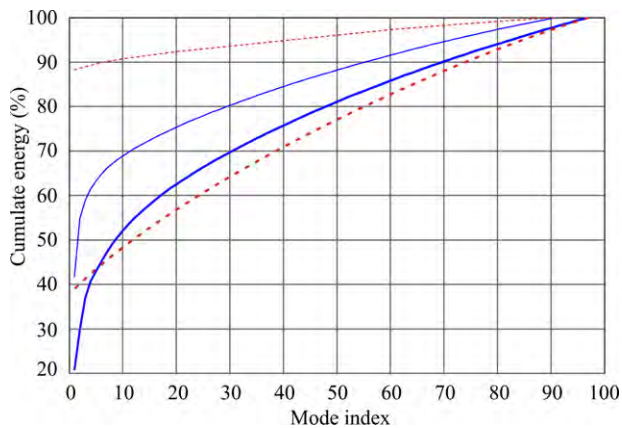


Fig. 2. Cumulate energy for POD of the velocity (continuous curves) and of the vorticity (dashed curves). Thin lines: Circular cylinder, $Re = 108$; Thick lines: Triangular cylinder, $Re = 94$.

the characteristic size of the obstacle (e.g. the edge length for a triangular cylinder) is of the order of a few grain diameters and reaches an asymptotic behavior for $d/b \ll 1$.

The circular cylinder experiments have already been analyzed in many aspects in [20], and most of the data herein reported refer to the case of triangular cylinder.

4. Results and discussion

4.1. Flow velocity fields

The cumulative energy of the modes in the POD analyses of two tests is shown in Fig. 2. For the circular cylinder, the POD analysis applied to the velocity gives a very energetic first mode, accounting for more than 40% of the total energy, but it is still necessary to include many other modes to reach 90% total energy. In comparison, the POD applied to the vorticity shows that the first mode accounts for 87% of the total energy and it requires less than 10 modes for reaching 90% of the energy. This behavior indicates that the vorticity in this specific flow field is much simpler and organized than the velocity field. The advantage is evident in those analyses directly using the vorticity, but it is not if the velocity is the ultimate goal. In fact, the only way to calculate the velocity field after knowing the vorticity is to integrate the Biot–Savart expression, which is computationally expensive, and no simple relationship can be found between the modes of velocity decomposition and those of vorticity decomposition. POD applied to the triangular cylinder (thick lines in Fig. 2) shows that, while the first five modes of vorticity still retain more energy than the corresponding modes for velocity, the higher order modes do not. Hence the vorticity pattern at higher order modes is more complex than the velocity patterns, and thus requires more modes to be properly described.

By considering only the modes retaining 90% of the energy, two flow fields with the triangular cylinder are computed and shown in Fig. 3.

A comparison between the experimental results herein, the numerical integration results for Newtonian fluids [35] and the experiments for a dry granular stream by [3] is shown in Fig. 4. Nedderman et al. experiments (hereafter NDH) were made in a vertical channel consisting of two vertical glass plates held 2.3 cm apart by wooden spacers and with a flow section 20 cm wide. All the observations were made using mustard seed of mean diameter 2.28 mm, with a static angle of repose equal to $\approx 32^\circ$ and with a few black kale seeds added to provide visible marker particles. The length of the edge of the base of the triangular cylinder was equal to

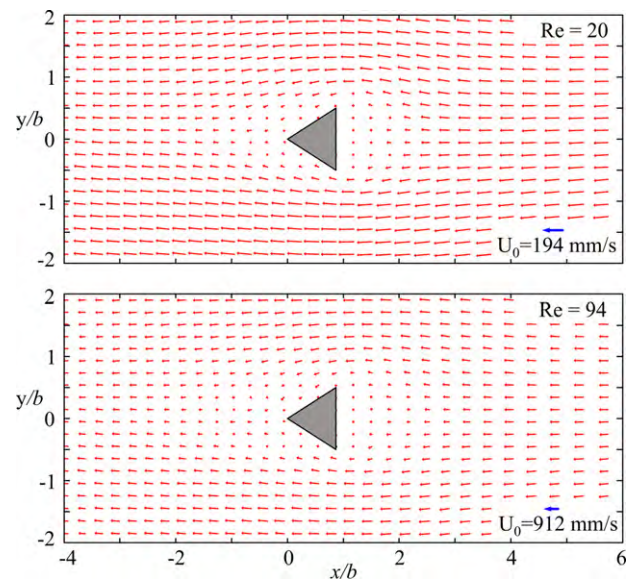


Fig. 3. Average velocity retaining 90% of the mode energy (100 couples of frames, ≈ 27 s) for tests at the minimum and maximum Reynolds number. The scale is different for the two tests and the vectors shown are halved in the vertical and reduced to one third in the horizontal direction for a better visualization. b is the length of the edge of the equilateral triangle.

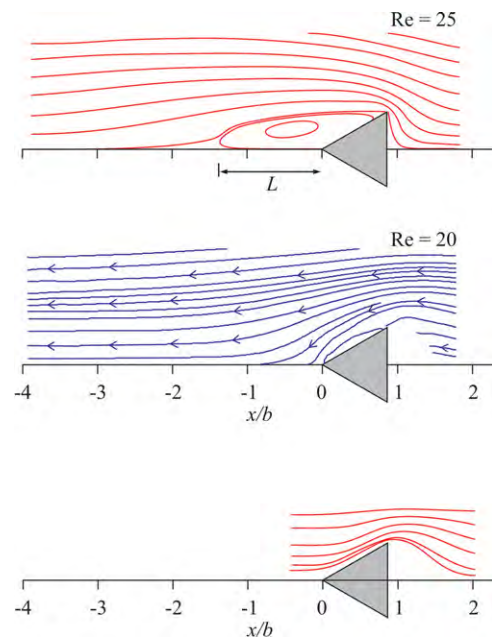


Fig. 4. Comparison between streamlines for a Newtonian fluid (upper panel, [35]), present experiments (mid panel) and dry granular flow (lower panel, [3]). L is the extension of the recirculating cell.

$b = 100$ mm hence it results $d/b = 2.28/100 = 0.0288$, accidentally equal to the ratio $d/b = 0.375/13 = 0.0288$ for the present experiments. Being difficult to evaluate the Reynolds number for a dry granular stream, the upstream velocity is considered as reference for comparison. For NDH tests the far field upstream velocity is equal to $U_0 = 0.81$ m/s, roughly corresponding to the present experiments at Reynolds number between 77 and 94. However, NDH also reported that the streamlines do not change significantly doubling the upstream velocity. Due to the geometry of NDH experiments, with the triangular body of side equal to half the channel width, the mean velocity in the plug flow between the lateral walls and the body is twice the upstream far field velocity. In the lower part of the parallel sided channels between the insert and

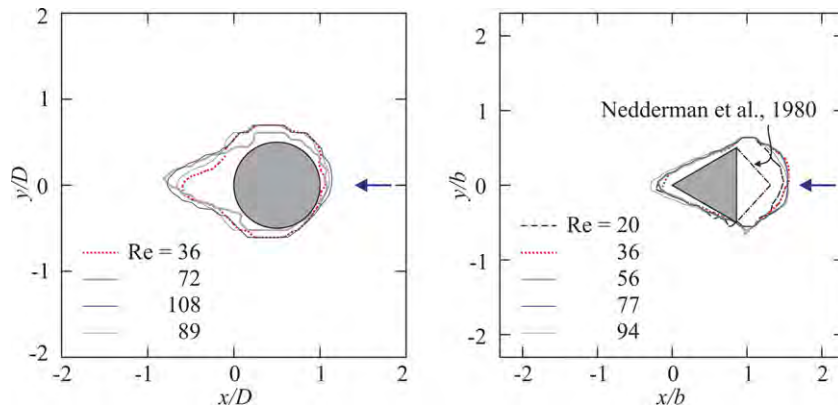


Fig. 5. Contour lines where velocity has dropped to 5% of the asymptotic velocity. Also [3] result for a dry granular stream is shown.

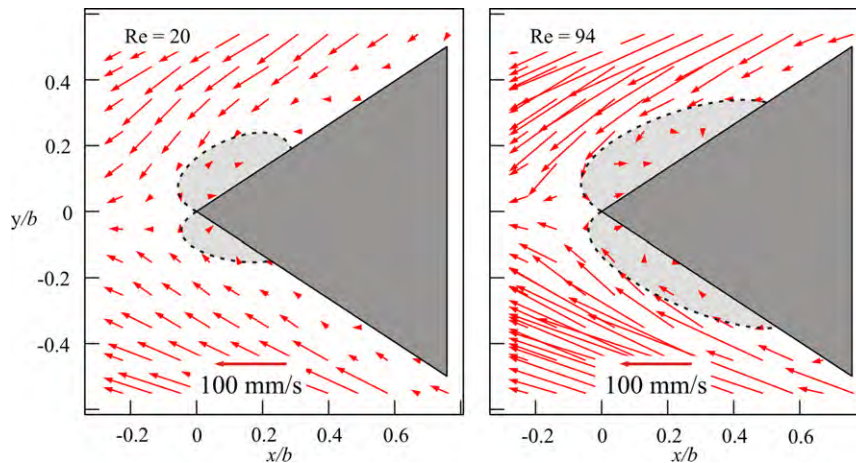


Fig. 6. Recirculation cells past the obstacle.

the wall, the streamlines were found to curve sharply following the side of the triangular body, without apparent re-circulation zone. Plug flow was rapidly re-established further up the channel.

An unexpected characteristic of the measured flow field in the present experiments and in the dry granular stream experiments is that the streamline patterns seem to suggest, at first sight, that flow is as one would expect for a fluid flowing in the opposite direction. Whereas, for a Newtonian fluid, the wake lies behind the object, the separation for a dry granular material and for a granular mixture is ahead of the object.

The presence of the obstacle modifies the flow patterns, with a low-velocity zone upstream, a stagnation or dead zone (sediment at rest) downstream, a boundary layer at the interface between the dead zone and the obstacle, and a wake. In Fig. 5, the contour lines of the 95% of the asymptotic velocity are presented. Note the significant difference in the velocity pattern near the two bodies. In the case of triangular cylinder, the region of sediment at rest is upstream and extends for $\approx 0.7b$. It is slightly dependent on the Reynolds number, and typically has a semi-circular shape. In the case of a circular cylinder, the thickness of the layer of sediment at rest is quite small immediately upstream, while there are two symmetric recirculation patterns downstream (see [20]), with an extension slightly dependent on the Reynolds number. For the triangular cylinder with a dry granular stream in NDH experiments it can be seen that upstream the triangular insert there was a large stagnant zone of approximately triangular shape, with inclination of the apparent boundary considerably larger than the static angle of repose of the particles; refer to Fig. 5. From NDH experiments with different shape of the obstacles and from the present tests

there is a convincing demonstration that the flow is controlled by factors downstream of the location of interest.

Past the obstacles, grains are shed off the solid surface and a separation occurs, apparently not present for a dry granular stream. This is also evident for Newtonian fluid, for which the critical Reynolds number for the onset of separation is around 12 [6]. Two almost symmetric re-circulation cells are reported (see Fig. 6), with size increasing with the Reynolds number. These cells are confined to the side of the triangle, whereas, for a Newtonian fluid, [35] showed that the length of the recirculation cells measured from the apex downstream can be computed as

$$L/b = -1.53 + 0.118Re, \quad 10 \leq Re < 35, \quad (21)$$

which results in much larger values than those measured in the present tests.

This behavior is also different than that observed for dry granular flows. For a cylinder in a dry granular flow stream [36,12], an empty region occurs downstream of the cylinder, because the limited granular temperature cannot overcome the particle inertia to push the grains in the transverse direction. Separation is thus a consequence of the inertia which dominates at high Reynolds number. In addition, non-cohesive grains cannot sustain any tensile load that develops at the trailing edge of the cylinder.

It is also different from that obtained through numerical computation for power-law fluids [6], who found that, for shear-thickening fluids, the critical Reynolds number for the onset of separation is $Re_c \approx 7$ with behavior index equal to 1.5.

For the granular mixture, the variation in sediment void concentration modifies the apparent local viscosity, significantly reducing the equivalent Reynolds number, where locally the

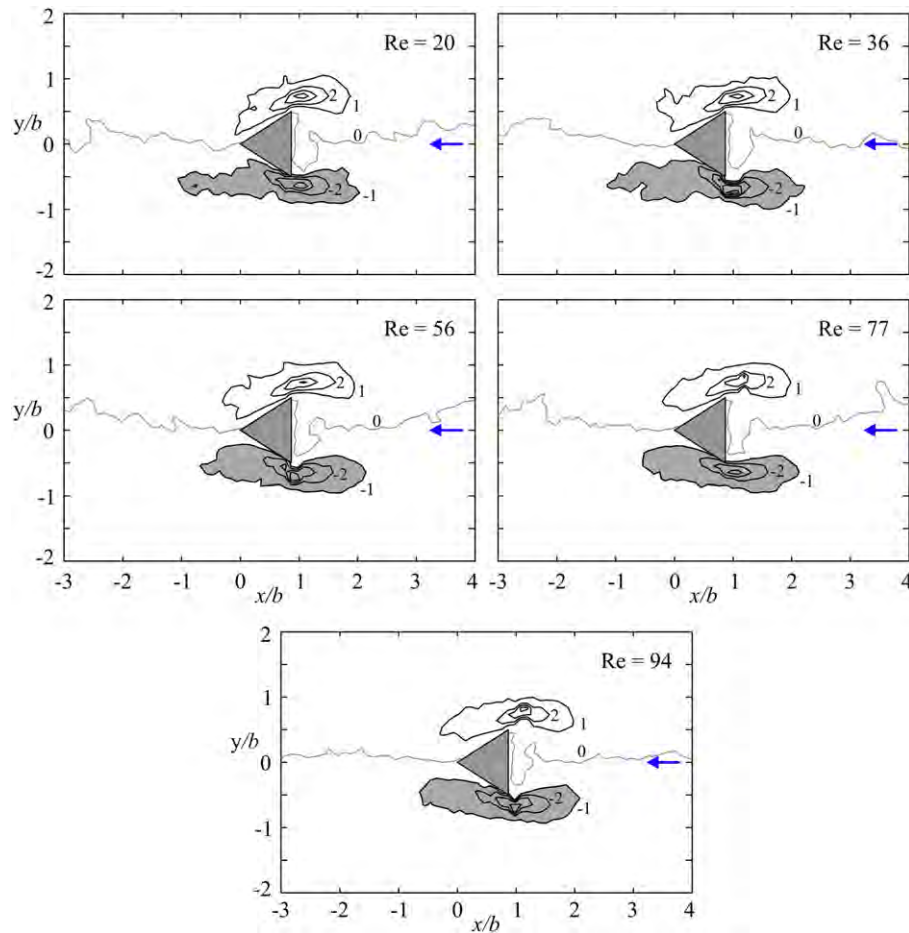


Fig. 7. Average non dimensional vorticity $\omega_z^* = \omega_z b / U_0$. The grey area represents the clockwise vorticity.

grain void concentration increases. Hence, the effective Reynolds number is much lower than the nominal one, based on the asymptotic velocity and on the average equivalent viscosity. The particles are at rest because a small pressure guarantees contact with the body and avoids detachment.

4.2. Vorticity

The flow field is essentially 2-D, so only the component ω_z of the vorticity can be measured. The average non-dimensional vorticity $\omega_z^* = \omega_z b / U_0$ is shown in Fig. 7. Two macro vortices are evident near the upper and lower separation points, with maximum intensity equal to $\approx \pm 4$, and geometry almost independent on the Reynolds number. A similar maximum value was also typical of circular cylinder [20].

The shape of the vortices is similar for all tests, and the vorticity contour line of $\omega_z^* = 1$ is confined within $[-b, 2b]$ streamwise. The pattern is symmetric about the centreline and extends also upstream of the base of the triangular cylinder. A comparison between the average vorticity distribution measured here and that computed for Newtonian fluid ([6,37]) is shown in Fig. 8. The main difference is the presence of strong vorticity upstream and the short extension of the vortices downstream in the measurement. The upstream vorticity is due to the sediment at rest at contact with the base of the obstacle, which tend to modify the shape of the triangle by adding a semi-circle at the base of the triangle (see Fig. 5). It does not happen for a Newtonian fluid, which shows intense vorticity at the apex of the obstacle but with limited extension near the base of the obstacle. The shorter distance downstream, where the vorticity generated near the body remains, can

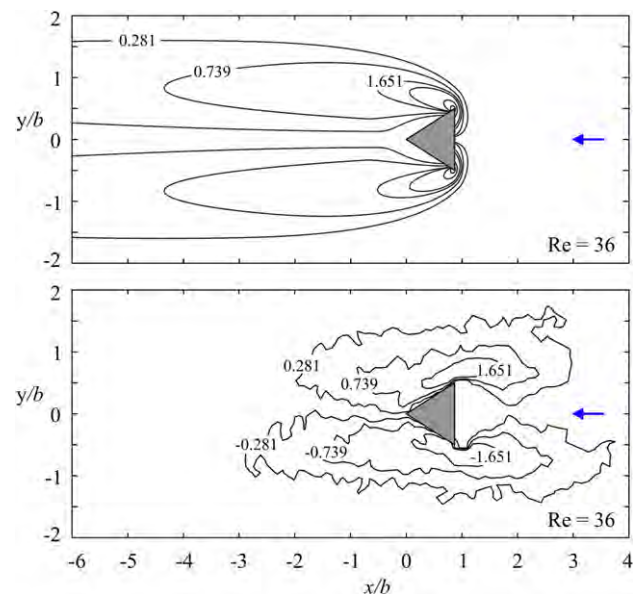


Fig. 8. Average non dimensional vorticity $\omega_z^* = \omega_z b / U_0$. Comparison between numerical results for a Newtonian fluid (upper panel, from [6] and [37]) and present experiments (lower panel).

be attributed to the much higher dissipation in the grain-water mixture than a Newtonian fluid, which cannot be properly quantified by considering only an equivalent viscosity of the mixture.

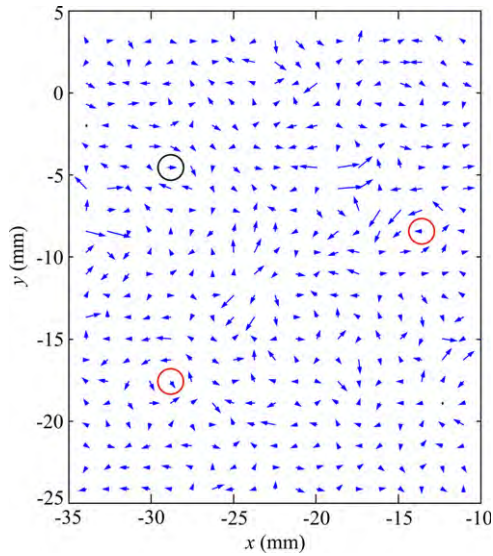


Fig. 9. High-pass filtered flow field for a single frame with three detected vortices having radius 2.5 mm. Test with triangular cylinder at $Re = 20$. The flow is from the right.

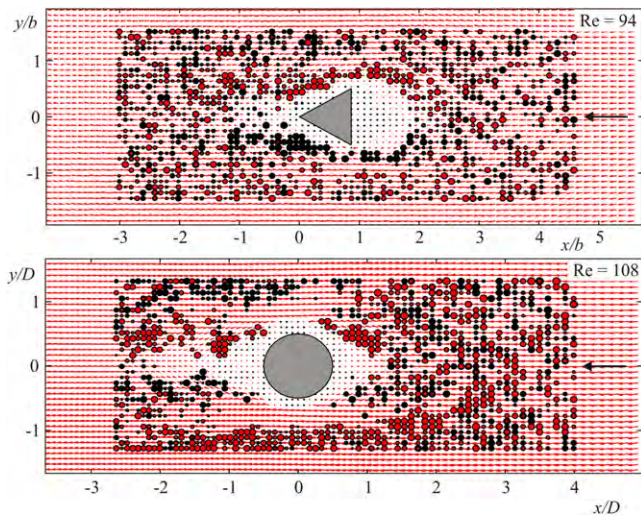


Fig. 10. Vortices detected for all frames. The size is proportional to the radius, arbitrary scale. Black: CW vortices; Grey (red): CCW vortices.

In the present conditions, no von Karman vortices develop, even though the frequency of acquisition can be a limiting factor in their detection.

4.3. The vortices

Fig. 9 shows a snapshot of the flow field after high-pass filtering with three vortices automatically detected. The analysis has been performed by setting a maximum radius of eddies to be 4 mm ($\approx 10d$).

Fig. 10 shows the spatial distribution of vortices, with the size of the circles representing vorticity proportional to their radius. A total of ≈ 1800 eddies were identified for the circular cylinder, and ≈ 2000 for the triangular cylinder, using 100 frames for each test (≈ 27 s). On average, there are 18–20 eddies per frame. Fig. 11 reports the location of vortices by circles, whose size is proportional to the energy (arbitrary scale). While some vortices are present far from the obstacle, those significantly energetic are by the obstacles in the boundary layer that marks the interface between sediment at rest and sediment at move. The circular

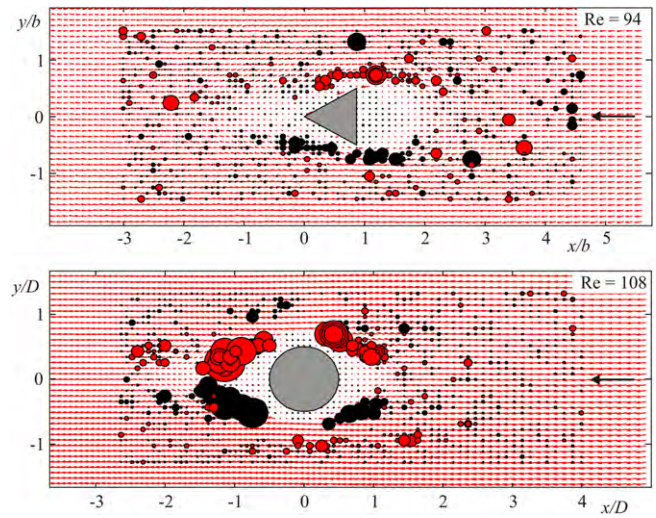


Fig. 11. Vortices detected for all frames. The size is proportional to the energy, arbitrary scale. Black: CW vortices; Grey (red): CCW vortices.

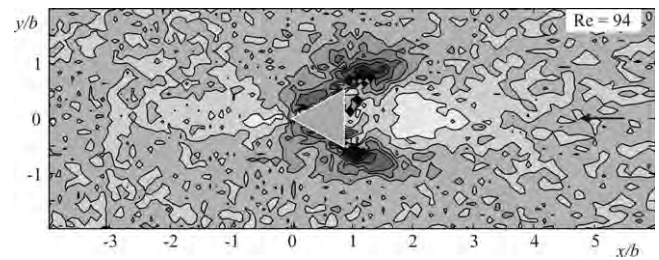


Fig. 12. Average distribution of the regions satisfying [32] criterion. The darkest regions refer to the maximum frequency.

cylinder leads to the generation of more energetic eddies with a gap in the separation area, where vorticity has a maximum (see [20]).

In order to reveal the effects of the λ_2 -criterion, Fig. 12 shows the spatial distribution of the frequency of occurrence of $\lambda_2 < 0$ for a single test; other tests show a similar pattern, and similar patterns are also observed for a circular cylinder. In a two-dimensional flow, it is essentially a tool to separate vorticity due to shearing and that due to swirling, and, in the present analysis, is a necessary but not sufficient condition for the existence of a vortex. The most likely areas for vortices are near the vertex of the base, where vorticity is also quite strong, whereas, for circular cylinder, the likely areas also include the shoulders of the obstacle, where vortices have not been detected.

Fig. 13 depicts the probability density function (pdf) for clockwise and counterclockwise vortices having radius equal to 2 mm at $Re = 94$. Counter-clockwise eddies, carrying positive vorticity, have a pdf similar to clockwise eddies, and only minor differences are observed partially due to a small asymmetry in the flow field and to the limited size of the sample used in the statistics. The distribution of the energy for varying radius is shown in Fig. 14. Similar findings are reported in [29]. The pdf of the vorticity is expected to be log normal for all eddies as a result of the product of a large number of independent, identically-distributed variables, and the peak decreases with increasing radii. For energy $\Gamma^2/U_0^2 b^2 \rightarrow 0$, a drop of all curves is reported. The energy should decrease with reduced size of the eddies, with a minimum at a radius equal to the Kolmogorov scale, which is less than the effective resolution of the present analysis (about 1.25 mm).

The pdfs of the vortices vs non dimensional energy are shown in Fig. 15 at varying Reynolds numbers. The peak reduces, and the distribution is also more uniform at lower Reynolds numbers.

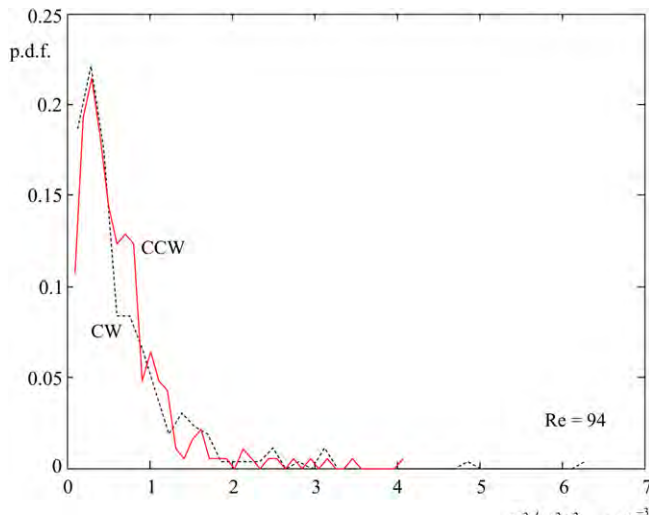


Fig. 13. Probability distribution of energy circulation for all detected vortices. Vortex radius, $r = 2$ mm. Vortices detected for test at $Re = 94$ triangular cylinder obstacle. Dashed line (black): CW vortices; bold line (red/grey): CCW vortices.

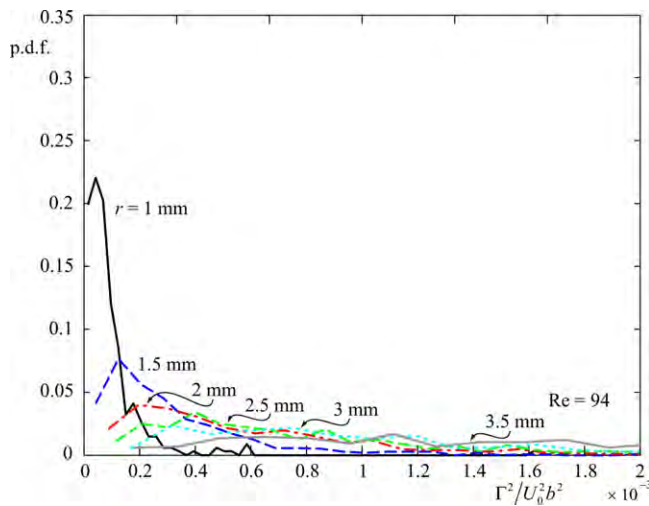


Fig. 14. Probability distribution of energy circulation for all detected vortices. Vortices detected for test at $Re = 94$, triangular cylinder.

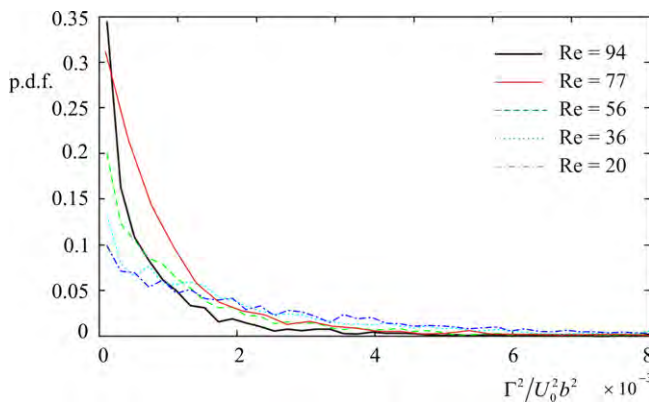


Fig. 15. Normalized energy as a function of the Reynolds number, triangular cylinder.

Larger Reynolds number favors smaller eddies, which are more dissipative. The energy contribution vs the size of eddies is shown in Fig. 16 for a single test at $Re = 94$ using the triangular cylinder

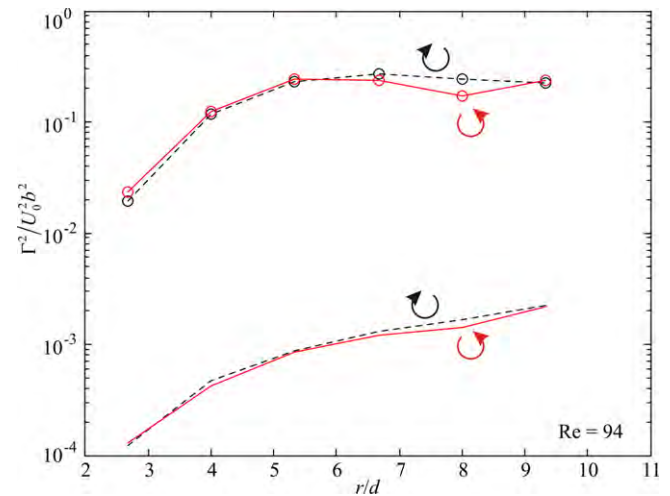


Fig. 16. Non dimensional mean energy of the vortices (bold and dashed curves) and total energy of the vortices (curves with symbols). Vortices detected for test at $Re = 94$, triangular cylinder obstacle.

obstacle. Both CW and CCW give equal contribution except for large eddies, where the CW ($\omega < 0$) eddies are dominant because they carry more energy per eddy (lower curves in Fig. 16) and are also more populous. The maximum is reached at $r/d \approx 6.6$ (2.5 mm), which represents the preferential size of the eddies at that Reynolds number. The same value is obtained for tests at other Reynolds numbers, even though a second maximum is also present for $r/d \approx 9.3$ (3.5 mm). For circular cylinder, the maximum is always at $r/d \approx 9.3$ (3.5 mm).

The population of the vortices is almost equally spread in the two half planes (Fig. 17), the upper plane where essentially $\omega > 0$ and the lower plane where $\omega < 0$. As expected, the energy contribution is dominated by CW eddies in the lower plane and by the CCW eddies in the upper plane. The differences in the energy contribution become negligible for eddies with radius equal or less than 2 mm, and it is coherent with a model of turbulence where smaller eddies tend to be isotropic whereas larger eddies have a size, energy and spatial distribution depending on the macroscales of the flow. The presence of eddies carrying an opposite vorticity respect to the dominant local vorticity can be explained in several ways. For example, the intrinsic random nature of turbulence can generate coherent structures different from the average.

5. Conclusions

We have obtained grain velocity measurements in a 2-D stream of a granular mixture, with water as the inter particles fluid, around a circular and a triangular cylinder, and different velocity of the stream. The set of experiments should be extended including different viscosity of the interparticles fluid, different relative size of the grains respect to the length scale of the obstacles, different static angle of repose of the grains and possibly different roughness of the lateral walls of the obstacles.

- The flow field is similar to that of a Newtonian fluid but streamlines are much as one would expect for a fluid flowing in the opposite direction. This last behavior is typical of dry granular stream, as reported by [3].
- Flow visualization shows a limited recirculation zone past a triangular cylinder, less extended than for a Newtonian fluid and absent for a dry granular stream. Similar results were also found for the circular cylinder [20].

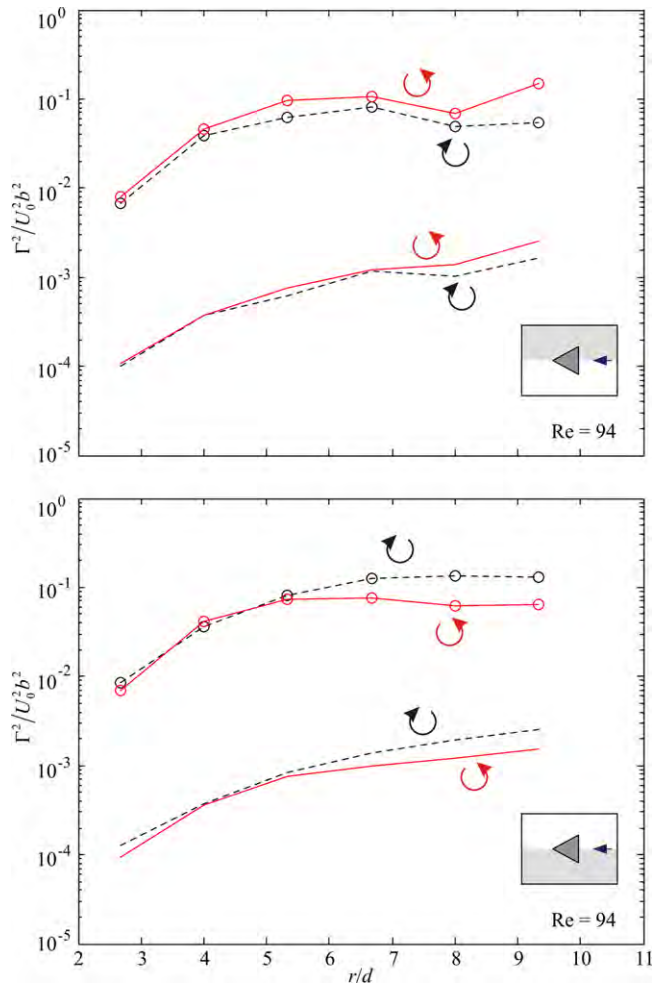


Fig. 17. Non dimensional mean energy of the vortices (bold and dashed curves) and total energy of the vortices (curves with symbols). Upper panel: upper half; lower panel: lower half. Vortices detected for triangular cylinder obstacle.

- For the triangular cylinder, a zone of sediment almost at rest is present upstream, with a semi-circular shape and an extension independent on the Reynolds number. This zone modifies the shape of the obstacle. Instead, the zone has a triangular shape for a dry granular stream [3] with edge inclination much larger than the static angle of repose of the grains.
- In Nedderman et al. experiments, carried out also with obstacles of different shape, there is a convincing demonstration that the flow is controlled by factors downstream the location of interest. The present tests show a similar behavior.
- The vorticity scales with the size of the obstacle and the asymptotic velocity. Vorticity is confined near the vertices of the base of the triangular cylinder and, respect to vorticity induced by a Newtonian fluid, it spreads more upstream. This is due to the zone of sediment almost at rest at the base of the triangle, which modify the apparent shape of the obstacle. The vorticity reaches a maximum intensity of around $4U_0/b$. A similar value was obtained also for the circular cylinder.
- The vortices vs their energy have a probability distribution function with a peak and a fast drop. The pdf of vortices vs. their normalized energy does not scale with the Reynolds number. The contribution of clockwise and counter-clockwise vortices is almost balanced.

Acknowledgments

This paper was written while SL was a visitor at the Cambridge University Engineering Department, Cambridge, UK, kindly hosted by Dr. Liang and a by-fellow at Churchill College, Cambridge.

Appendix. Supplementary data

Supplementary material related to this article can be found online at <http://dx.doi.org/10.1016/j.euromechflu.2012.11.001>.

References

- [1] M.M. Zdravkovich, *Flow Around Circular Cylinders*, Vol. 1: Fundamentals, Oxford University Press, Oxford, UK, 1997.
- [2] T. Sarpkaya, P.G. Rainey, R.E. Kell, Flow of dilute polymer solutions about circular cylinders, *J. Fluid Mech.* 57 (1973) 177–208.
- [3] R.M. Nedderman, S.T. Davies, D.J. Horton, The flow of granular materials round obstacles, *Powder Technol.* 25 (1980) 215–223.
- [4] G. Pilate, M.J. Crochet, Plane flow of a second-order fluid past submerged boundaries, *J. Non-Newton. Fluid Mech.* 2 (1977) 323–341.
- [5] A.K. De, A. Dalal, Numerical simulation of unconfined flow past a triangular cylinder, *Int. J. Numer. Methods Fluids* 52 (2006) 801–821.
- [6] A. Prashanna, A.K. Sahu, R.P. Chhabra RP, Flow of power-law fluids past an equilateral triangular cylinder: momentum and heat transfer characteristics, *Int. J. Therm. Sci.* 50 (2011) 2027–2041.
- [7] S. El-Sherbiny, Flow separation and reattachment over the sides of a 90° triangular prism, *J. Wind Eng. Ind. Aerodyn.* 11 (13) (1983) 393–403.
- [8] G. Buresti, G. Lombardi, A. Talamelli, Low aspect-ratio triangular prisms in cross-flow: measurements of the wake fluctuating velocity field, *J. Wind Eng. Ind. Aerodyn.* 74–76 (1998) 463–473.
- [9] G.V. Iungo, G. Buresti, Experimental investigation on the aerodynamic loads and wake flow features of low aspect-ratio triangular prisms at different wind directions, *Journal of Fluids Structures* 25 (2009) 1119–1135.
- [10] M.E. Ali, O. Zeitoun, A. Nuhait, Forced convection heat transfer over horizontal triangular cylinder in cross flow, *Int. J. Therm. Sci.* 50 (2011) 106–114.
- [11] C.R. Wassgren, J.A. Cordova, R. Zenit, A. Karion, Dilute granular flow around an immersed cylinder, *Phys. Fluids* 15 (11) (2003) 3318–3330.
- [12] D. Chehata, R. Zenit, C.R. Wassgren, Dense granular flow around an immersed cylinder, *Phys. Fluids* 15 (6) (2003) 1622–1631.
- [13] K. Wieghardt, Experiments in granular flow, *Annu. Rev. Fluid Mech.* 7 (1975) 89–114.
- [14] V. Buchholtz, T. Pöschel, Interaction of a granular stream with an obstacle, *Granular Matter* 1 (1998) 33–41.
- [15] J.M.N.T. Gray, Y.-C. Tai, S. Noelle, Shock waves, dead zones and particle-free regions in rapid granular free-surface flows, *J. Fluid Mech.* 491 (2003) 161–181.
- [16] S. Longo, A. Lamberti, Granular shear flow mechanics, *Exp. Fluids* 32/3 (2002) 313–325.
- [17] R. Deng, C.-H. Wang, Particle image velocimetry study on the pattern formation in a vertically vibrated granular bed, *Phys. Fluids* 15 (2003) 3718–3729.
- [18] R.A. Bagnold, Experiments on a gravity free dispersion of large solid spheres in a Newtonian fluid under shear, *Proc. R. Soc. A* 225 (1954) 49–63.
- [19] M.L. Hunt, R. Zenit, C.S. Campbell, C.E. Brennen, Revisiting the 1954 suspension experiments of R. A. Bagnold, *J. Fluid Mech.* 452 (2002) 1–24.
- [20] S. Longo, A. Valiani, L. Lanza, Experiments on the two-dimensional flow of a grain-water mixture past a circular cylinder, *Eur. J. Mech. B/Fluids* 36 (2012) 139–151. Elsevier.
- [21] P. Jalali, Flow characteristics and stresses on cylindrical objects immersed in a flow of inelastic hard disks, *Powder Technol.* 219 (2012) 217–227.
- [22] D. Liang, C. Jiang, Y. Li, Cellular neural network to detect spurious vectors in PIV data, *Exp. Fluids* 34 (1) (2003) 52–62.
- [23] J.L. Lumley, *Stochastic Tools in Turbulence*, Academic Press, London, 1970.
- [24] L. Sirovich, Turbulence and the dynamics of coherent structures. Parts I, II and III, *Q. Appl. Math.* XLV (3) (1987) 561–582.
- [25] P. Holmes, J.L. Lumley, G. Berkooz, *Turbulence, Coherent Structures, Dynamical Systems and Symmetry*, Cambridge University Press, 1996.
- [26] L. Sirovich, Chaotic dynamics of coherent structures, *Phys. D* 37 (1989) 126–145.
- [27] J. Kostas, J. Soria, M.S. Chong, A comparison between snapshot POD analysis of PIV velocity and vorticity data, *Exp. Fluids* 38 (2) (2005) 146–160.
- [28] S.K. Robinson, S.J. Kline, P.R. Spalart, Quasi-coherent structures in the turbulent boundary layer — II: Verification and new information from a numerically simulated flat-plate boundary layer, in: S.J. Kline, N.H. Afgan (Eds.), *Near Wall Turbulence, Proceedings of Zaric Memorial Conference*, Hemisphere, New York, 1989, pp. 218–247.
- [29] A. Agrawal, A.K. Prasad, Properties of vortices in the self-similar turbulent jet, *Exp. Fluids* 33 (2002) 565–577.
- [30] A.E. Perry, M.S. Chong, A description of eddy motions and flow patterns using critical-point concepts, *Ann. Rev. Fluid Mech.* 19 (1987) 125–155.
- [31] A.K.M.F. Hussain, Coherent structures and turbulence, *J. Fluid Mech.* 173 (1986) 303–356.
- [32] J. Jeong, F. Hussain, On the identification of a vortex, *J. Fluid Mech.* 285 (1995) 69–94.
- [33] L. Graftieux, M. Michard, N. Grosjean, Combining PIV, POD and vortex identification algorithms for the study of unsteady turbulent swirling flows, *Meas. Sci. Technol.* 12 (2001) 1422–1429.

- [34] G.I. Taylor, Stability of viscous liquid contained between two rotating cylinders, *Phil. Trans. R. Soc. A* 223 (1923) 289–343.
- [35] O. Zeitoun, M. Ali, A. Nuhait, Convective heat transfer around a triangular cylinder in an air cross flow, *Int. J. Therm. Sci.* 50 (2011) 106–114.
- [36] J.-C. Tsai, W. Losert, G.A. Voth, J.P. Gollup, Two-dimensional granular Poiseuille flow on an incline: multiple dynamical regimes, *Phys. Rev. E* 65 (2002) 011306.
- [37] R.P. Chhabra, 2012 (Personal communication).